UV curable nanocomposites with tailored dielectric response

C. Mendes-Felipe[1,2], T. Rodrigues-Marinho[3], José L. Vilas[1,2], S. Lanceros-Mendez[1,4]

[1]BCMaterials, Basque Center for Materials, Applications and Nanostructures, UPV/EHU Science Park, 48940 Leioa, Spain

[2]Macromolecular Chemistry Group (LABQUIMAC), Department of Physical Chemistry, Faculty of Science and Technology, University of the Basque Country (UPV/EHU), Barrio Sarriena s/n, E-48940 Leioa, Spain

[3]Center/Department of Physics, University of Minho, Campus of Gualtar, 4710-057 Braga, Portugal

[4]IKERBASQUE, Basque Foundation for Science, 48013, Bilbao, Spain

Graphical Abstract

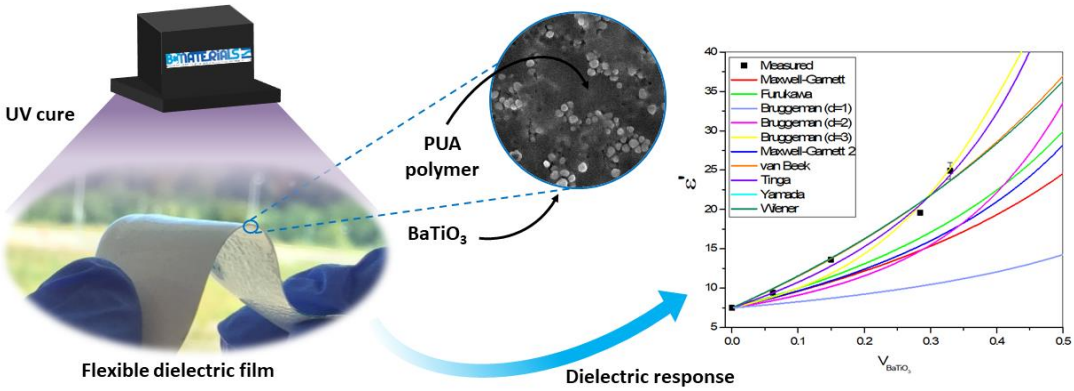

Abstract

Photopolymerization or UV curing represents a fast and solvent-free technique to obtain polymer-based composites, being one of the main methods used in lithographic processes, surface coatings and the manufacture of integrated circuits. This work reports on the development of UV curable barium titanate/ polyurethane acrylate ($BaTiO_3$/PUA) composites with varying ceramic contents in order to tailor the dielectric response of the material. A good dispersion of the ceramic particles within the polymer matrix is obtained, together with a thermal stability of the composites up to 160 ºC. The inclusion of the $BaTiO_3$ nanoparticles onto PUA photoresin slightly decrease the glass transition temperature of the organic matrix. The obtained white coloured films show mechanical flexibility with elongations at break up to 25%. The increase of $BaTiO_3$ content leads to an increase of the dielectric constant up to 25 for sample with 65 wt% content. The size of the $BaTiO_3$ nanoparticles proved not to be a key factor on determining the dielectric constant value of the composite for filler sizes up to 100 nm. Theoretical studies demonstrate that the model that better predict the behaviour of the $BaTiO_3$/PUA composites is the Tinga model, giving insights on the physical phenomena determining the dielectric response of the materials. Thus, high dielectric UV curable composites are obtained suitable for microelectronics applications.

Keywords

Polymer composites, UV curing; polyurethane acrylate photoresin; barium titanate; dielectric properties

Introduction

Technology is nowadays increasingly driven by the Industry 4.0 concept that includes and takes advantages of the Internet of things (IoT), cyber-physical systems and the Internet of services (IoS) [1,2].

IoT represents the network that allows a dynamic connection between different everyday objects [3,4], this system allowing digitalization and computerization of daily tasks and, therefore, energy saving, increased security and improved quality of life, among others [5].

Further, in order to achieve full development and improved performance, IoT and Industry 4.0 still need the development of advanced -smart and multifunctional- materials and production methods [6–8].

In this context, flexible electronics composed by organic and inorganic nano-structured materials show the necessary requirements for IoT applications: mechanically flexible devices, possibility to be implemented in large areas, conformable in different sizes and shapes, low cost and flexible fabrication methods and lower environmental impact [9,10]. Thus, a large variety of materials have been investigated as appropriate materials for IoT related devices, including thermoelectric materials [11], wearable antennas for autonomous communication and sensing [12], or piezoelectric, magnetostrictive, and magnetoelectric materials for sensing and energy harvesting applications [7,8,13–15].

Directly related with the production of flexible electronics, printing techniques emerge as suitable approach as they allow the additive manufacturing deposition on large areas in rigid as well as flexible or irregular surfaces of (multi)functional materials [8,16]. In particular, among the different printing techniques, non-contact methods such as inkjet printing, laser-induced forward transfer or aerosol-jet printing can transfer inks to substrates without damage or contamination risks [17]. Therefore, they enable material deposition on irregular surfaces and are attractive for the production of printed electronics [18–20].

Printed electronics has been traditionally focusing on conductive materials [21–24]. Nevertheless, passive electronic components are essential for the fabrication of sensing and/or wireless systems and devices. In fact, the printing of those passive components will improve device integration, as passive electronic components, including capacitors or coils, are still the most voluminous parts of the current printed electronic circuits [25].

Electronic circuits require very specific functional characteristics, and this continues to be a challenge for printing techniques. In order to overcome this challenge, two different approaches

can be distinguishing: process engineering where the currently existing materials are tailored in terms of shape, geometry and interconnectivity [25], or material engineering where new materials with tailored functional characteristic for each application (such as electrical conductivity or dielectric constant) are developed.

In particular, for dielectric materials, the main approach for tailoring dielectric constant is to include large dielectric constant ceramic particles into polymeric matrix [26]. Polymers offer advantages such as easy processability or good mechanical properties, while ceramic particles provide high dielectric features [27]. Further, composite with related properties such as piezoelectric, pyroelectric or ferroelectric properties can be also processed [8]. The most used ferroelectric ceramic for this purpose is barium titanate, $BaTiO_3$, crystallizing in perovskite structure, as it is a lead free ceramic with high dielectric constant (ε), depending on its purity, grain size, temperature or preparation method [28,29]. In the case of polymers, polymethylmethacrylate [30], polyetheretherketone (PEEK) [31], polystyrene [32], or polyvinylidene fluoride (PVDF) [33,34] have been used for the developments of those composites.

In the context of materials for printed electronics, photopolymerizable or UV curable polymers emerge as a good alternative to solvent or melting processing due to the advantages of photopolymerization process, including room curing temperature, curing times of minutes or seconds, reduced VOC emissions and space and energy efficiency, among others [7]. Up to now, just a few studies on UV curable dielectric materials have been reported, mainly focussing on the electrical properties of the materials. Among them, polyethylene glycol diacrylate composites with $BaTiO_3$ particles with two different sizes and filler concentrations up to 50 wt% has been developed [27], as well as composites based on UV-curable resin Loctite® with Ag and $BaTiO_3$ nanoparticle content up to 56.2 vol% [35], leading to films with dielectric constants between 25 and 300, depending the filler size and concentration. It is to notice that relevant parameters such as mechanical ones or in.depth theoretical modelling/interpretation of the observed behaviours have not been reported for these or related systems.

In this work, UV curable $BaTiO_3$ based nanocomposites with tailored dielectric response have been developed. The influence of the barium titanate content and size were evaluated in terms of morphological, thermal, mechanical and dielectrical properties of the composites. Further, the effect of the inclusion of the filler in the curing process of the polymer has been assessed as well as a theoretical evaluation providing insights on the relevant interactions determining the experimental dielectric results.

Experimental

Materials

Polyurethane acrylate (PUA) photoresin SPOT-E™ (SPOT-A Materials®) was selected as the UV curable polymer matrix. Barium titanate ($BaTiO_3$) nanopowder with three different grain sizes (50-70 nm, 100 nm and 200 nm) were used as fillers for the preparation of the composite films. All powders showed a purity of 99.9% and a density of 5.85 g/cm^3, were provided by SkySpring Nanomaterials, Inc. 2-Propanol (99.9%, Octopus® fluids) was used as sample cleaner. All composites samples were processed using the $BaTiO_3$ and the photoresin as received.

Samples preparation

The samples were prepared mixing different amounts of the barium titanate particles of 100 nm size with the corresponding volume of the polyurethane acrylate (PUA) resin to obtain 0, 20, 40, 60, 65 wt% $BaTiO_3$ content samples. Samples with 40 wt% content and barium titanate powders of 50-70 nm and 200 nm sizes have been also prepared. To promote a good dispersion of the barium titanate particles, the samples were placed in an ultrasound bath (ATU® ATM series Model ATM3L) during 5 h at a temperature of 30ºC. Then, samples were magnetically stirred at room temperature for 1h. After a complete dispersion was obtained, flexible films were prepared using doctor blade technique on a clean glass substrate. The samples were cured at room temperature for 5 minutes with a UV-LEDs lamp (405 nm wavelength, 50 mW/cm^2 of irradiance). Figure 1 shows the schematic process of the PUA and $BaTiO_3$/PUA composites preparation. Highly flexible composite films with a thickness around 250 µm were obtained, determined by a coater measurement gauge Fisher DualScope MPOR. Samples were stored at room temperature in the absence of illumination for further studies. The prepared samples are summarized in Table 1.

Table 1 – Nomenclature and composition of the prepared samples.

Sample	PUA resin (wt%)	50-70nm $BaTiO_3$ (wt%)	100nm $BaTiO_3$ (wt%)	200nm $BaTiO_3$ (wt%)
PUA0	100	-	-	-
PUA20_100	80	-	20	-
PUA40_50	60	40	-	-
PUA40_100	60	-	40	-
PUA40_200	60	-	-	40
PUA60_100	40	-	60	-
PUA65_100	35	-	65	-

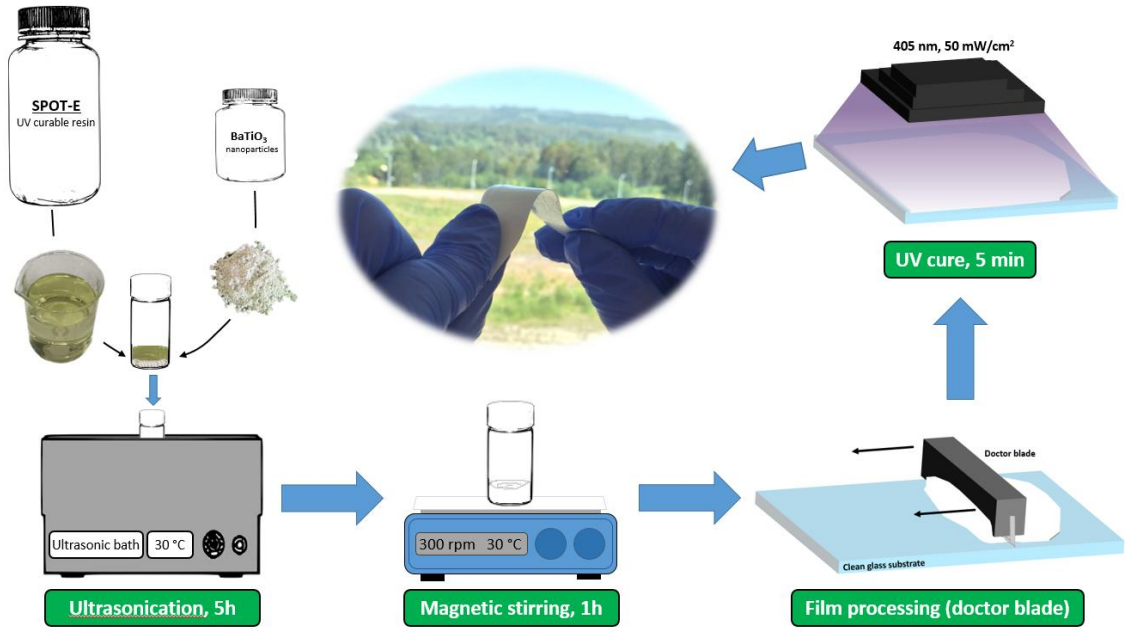

Figure 1 – Schematic representation of the preparation procedure of neat PUA and the corresponding $BaTiO_3$/PUA composites films.

Sample characterization

The evaluation of the photopolymerization reaction was carried out by Fourier transform infrared spectroscopy (FTIR) in a Thermo Nicolet Nexus 670 at the same time as the sample was illuminated with a UV laser at 405 nm. To perform the measurements, one drop of the different samples was deposited onto a KBr pellet and the absorbance spectrum as a function of time (one spectra per second, between 0 and 20 minutes) was collected in the spectral range from 4000 to 400 cm^{-1} with a spectral resolution of 4 cm^{-1}. The photopolymerization reaction was evaluated by monitoring the decrease in the absorbance of the double bond group centred at 1635 cm^{-1}. The conversion degree (α) of these double bonds was calculated considering the absorbance at 1635 cm^{-1} normalized with the carbonyl peak centred at 1730 cm^{-1}, according to equation (1) [36]:

$$\alpha = \frac{(A_{C=C}/A_{C=O})_{t_0} - (A_{C=C}/A_{C=O})_t}{(A_{C=C}/A_{C=O})_{t_0}} \quad (1)$$

The dispersion of the barium titanate fillers within the polymer matrix was evaluated by Scanning Electron Microscopy (SEM). The images on the cross-section of the cold fractured samples were obtained in a Hitachi S-4800 scanning electron microscope at accelerating voltage of 10 kV with magnifications of 400× and 5000×. Fourier transform infrared spectroscopy in the total attenuated reflection mode (FTIR-ATR) was also used to study the possible interactions between the polymer and the nanofillers. Measurements were performed with a Nexus FTIR Nicolet spectrophotometer in the spectral range of 4000 to 600 cm^{-1} with a spectral resolution of 4 cm^{-1} and 64 scans.

The thermal stability of the samples was evaluated by thermogravimetric analysis (TGA) in a Mettler Toledo TGA/SDTA851 instrument. The tests were performed from room temperature to 800 ºC, at heating rate of 10 ºC min^{-1} under nitrogen atmosphere. Two parameters were obtained from the thermograms: the degradation temperature (T_{deg}), measured as the extrapolated onset of the curve, and the temperature of maximum degradation rate (T_{max}), calculated as the first derivative peak temperature.

The effect of the inclusion of the fillers on the thermal transitions (glass transition temperature, T_g) of the polymer was evaluated by differential scanning calorimetry (DSC). Experiments were carried out using a DSC 822e from Mettler Toledo from -50 to 250 ºC at a rate of 20 ºC min^{-1} under nitrogen atmosphere in two successive scans. The glass transition temperature was calculated as the extrapolated onset of the baseline shift.

Mechanical properties were evaluated with a universal testing machine Shimadzu model AG-IS with a load cell of 1 kN. Measurements were performed at room temperature, in tensile mode, at a velocity of 3 mm min^{-1}, in samples with dimensions of 30 mm x 10 mm and an average thickness of 250 μm. The secant modulus (E) of the samples (calculated from the slope of the linear region), the maximum stress (σ_b) and the strain at break (ε_b) were determined. The values reported represent the mean average value and the standard deviation over 5 specimens.

The dielectric properties were obtained after measuring the capacity, C, and the dielectric losses, tan δ, at room temperature. An automatic Quadtech 1929 Precision LCR meter was used in frequency scans between 100 Hz and 1 MHz at an applied voltage of 0.5 V. Measurements were performed in samples in the parallel plate condenser approximation and thus, two circular gold electrodes of 5 mm diameter were deposited onto both sides of the samples by magnetron sputtering Quorum Q150T SC502 sputter coater. The real part of the relative permittivity or dielectric constant (ε´) was calculated by applying equation (2) [37]:

$$\varepsilon' = \frac{C \cdot d}{A} \qquad (2)$$

where C is the measured capacity, d is the thickness of the sample and A is the area of the gold deposited electrodes.

Results and discussion

Photopolymerization process

The photopolymerization reaction conversion (α) as a function of the exposure time for the pristine resin and the prepared samples is shown in Figure 2a (filler content dependence) and Figure 2b (filler size dependence). It is observed that increasing barium titanate content and size induce an important decrease on acrylic double bond conversion. Thus, the absorption of the

UV light by the ceramic powder induces a decrease of the light absorption by the photoinitiator and consequently, a decrease on the photopolymerization and conversion rate [27,36,38].

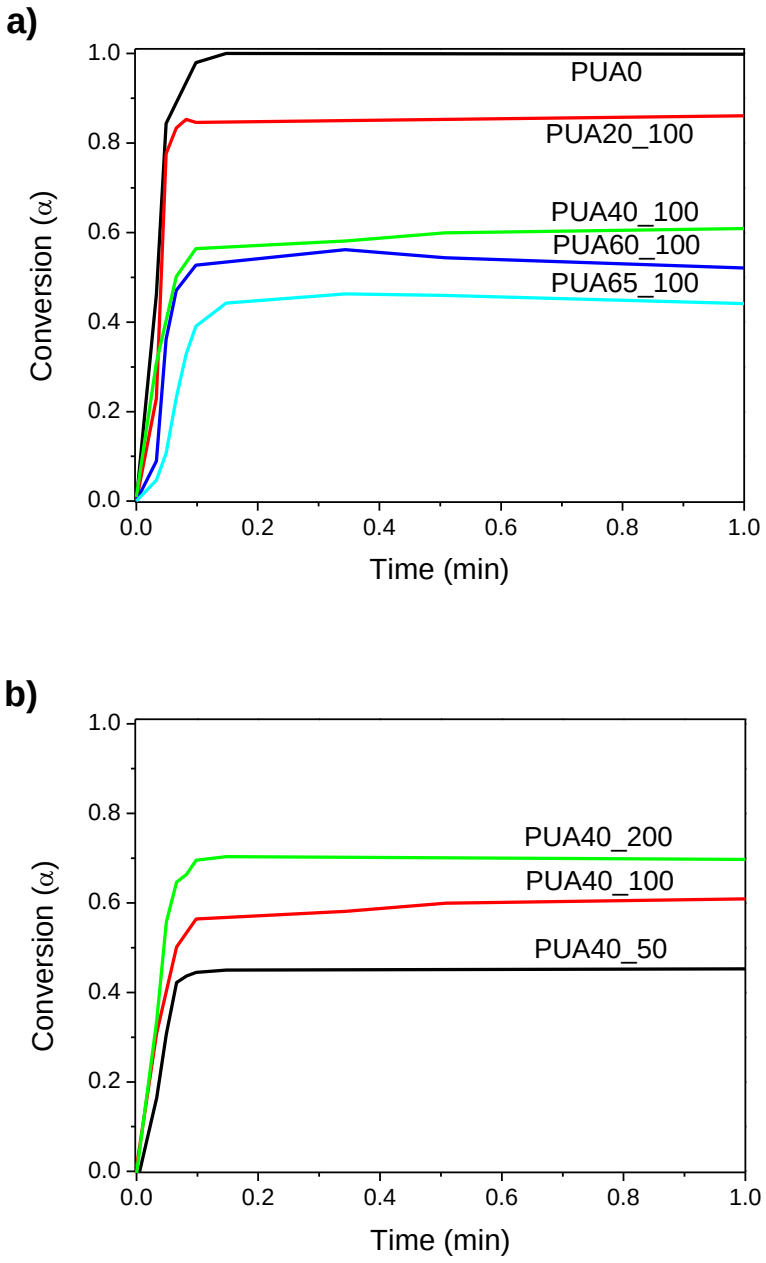

Figure 2 - Curing conversion of PUA and $BaTiO_3$/PUA composites for different nanoparticle content (a) and size (b).

It is important to notice that the maximum conversion is achieved in less than 1 minute for both PUA photoresin and composites, with a maximum conversion close to 100% for pristine resin and decreasing to 40% for the PUA65_100 composite, the one with the maximum $BaTiO_3$ content. This decrease of the acrylic double bond conversion [27] is related with the efficiency of the radical photoinitiator, which can be measured in terms of quantum yields of initiation and

quantum yields of polymerization. The absorption of UV light by barium titanate particles decrease the amount of light absorbed by the photoinitiator decreasing therefore the efficiency of the radical photoinitiator and, as a consequence, the obtained final conversion.

Morphological and chemical characterization

The dispersion and distribution of the $BaTiO_3$ particles into the PUA photoresin has been studied using the SEM images of the cross-section of the samples with nanofiller contents between 0 to 65 wt% and different filler sizes shown in Figure 3.

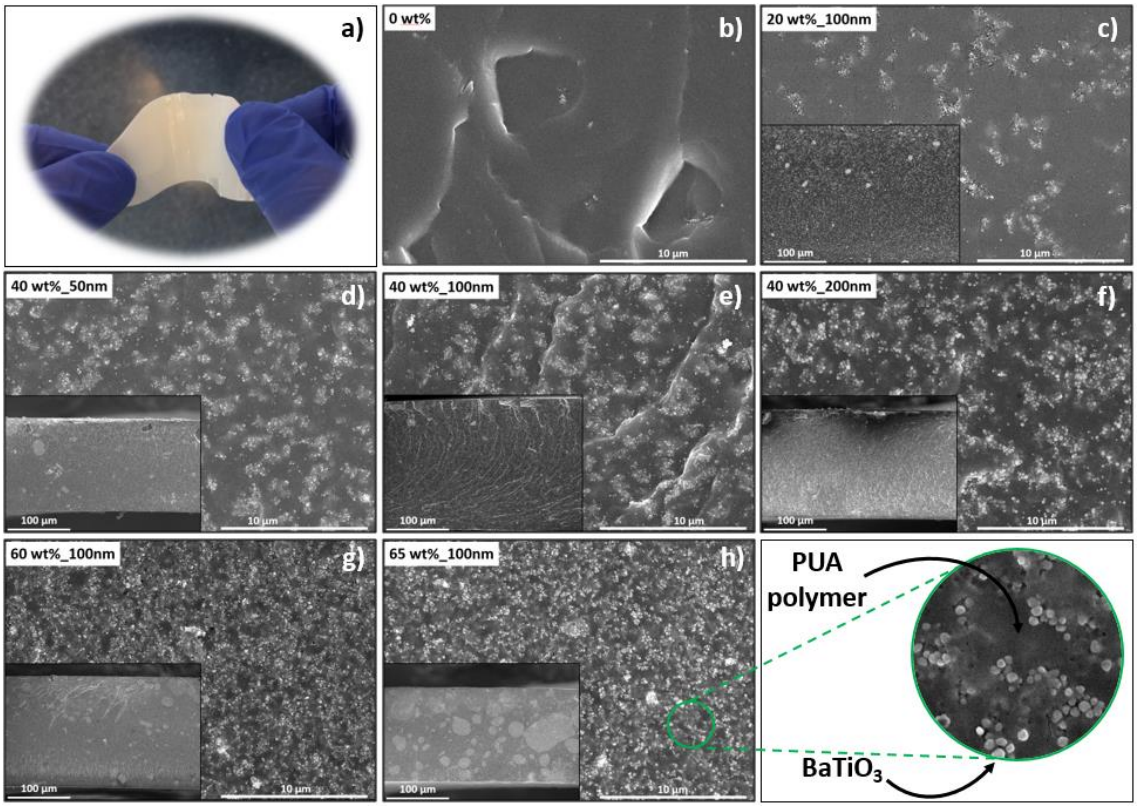

Figure 3 - Optical photograph showing the bendability and the macroscopic appearance of composite samples (a). Representative scanning electron microscopy (SEM) images at magnifications of 400x and 5000x of the cross-section of samples PUA0 (b), PUA20_100 (c), PUA40_50 (d), PUA40_100 (e), PUA40_200 (f), PUA60_100 (g), PUA65_100 (h).

In polymer nanocomposites, a suitable dispersion of the filler into the matrix is desirable as it affects electrical and mechanical properties [39,40]. SEM images (Figure 3) demonstrate the good dispersion of the $BaTiO_3$ particles within the PUA matrix up to 40 wt% concentration: no large agglomerates or voids are observed and good wettability of the filler by the matrix is verified.

On the other hand, samples with higher concentration of barium titanate particles (60 wt% or above) show larger agglomerates (insets of Figure 3g and h). Despite those agglomerates, $BaTiO_3$ particles are well dispersed along the samples (bright dots). Similar results for photopolymerized $BaTiO_3$-acrylic composites have been reported [27]. With respect to filler

size, results are similar for average filler sizes of 100 nm and 200 nm (Figure 3e and f), whereas barium titanate nanoparticles of 50-70 nm size, show larger well dispersed agglomerates (Figure 3d).

Fourier transformed infrared spectroscopy (FTIR) allows to evaluate possible physico-chemical interactions between the polymer matrix and the filler as well as to study the conformational properties of the obtained composites. Figure 4 shows the FTIR spectra of pristine photoresin and the prepared composites with different filler sizes and contents in the range of 4000 to 600 cm^{-1}. The polymer shows the characteristics peaks of the polyurethane acrylate, N-H stretching at 3330-3400 cm^{-1}, between 2855 and 2955 cm^{-1} the CH_2 and CH_3 stretch, C=O stretching at 1725 cm^{-1}, combined stretching of C-N and N-H bonds of the polyurethane group at 1550 cm^{-1}, C-N stretching at 1360 cm^{-1} and the C-O-C stretching at 1110 cm^{-1} [41].

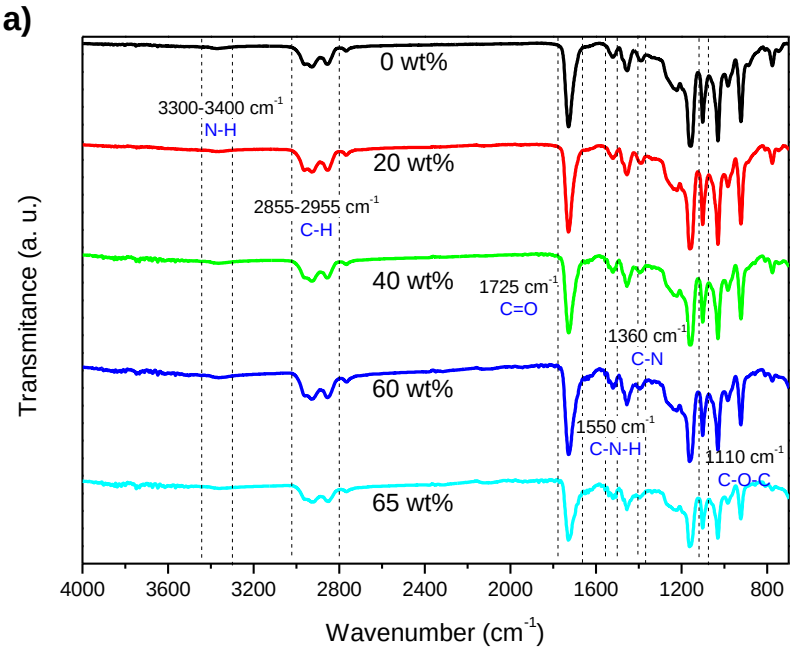

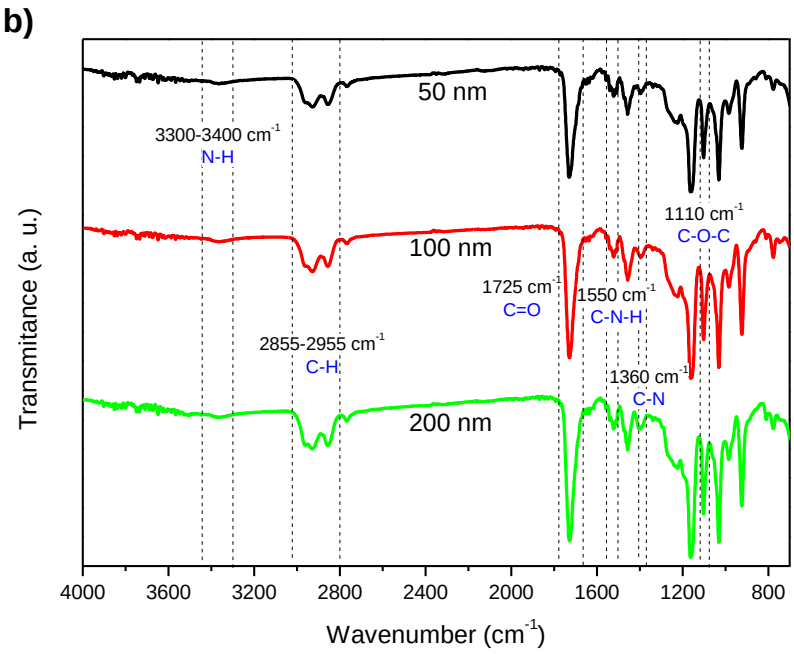

Figure 4 - Fourier Transformed Infrared (FTIR) spectra for PUA resin and corresponding composites with varying $BaTiO_3$ content (a) and size (b).

The spectra as similar for the polymer matrix and the composites: no band displacement or the appearance of new peaks are observed upon the addition of barium titanate particles, indicating no intermolecular interactions between the PUA polymer and the $BaTiO_3$ nanoparticles, independently of the filler content or size.

Thermal characterization

Thermogravimetric analyse (TGA) and Differential Scanning Calorimetry (DSC) were used to characterize the thermal properties of the composites in terms of the variations of the thermal degradation and glass transition temperatures, respectively, as a function of filler size and content.

Figure 5a shows the thermogravimetric (TG) and the differential thermal gravimetric (DTG) curves for PUA photoresin and the prepared composites for different $BaTiO_3$ content. TG and DTG for samples with different nanoparticle sizes are show in Figure 5b. The thermal degradation of neat polyurethane occurs in three steps: the first one in the temperature range of 160-280 ºC, the second one at 280-400 °C and the third step at 400-450 °C [41]. Residual monomers and physically absorbed solvent caused the first small decomposition step. The second step is assigned to the decomposition of the main polymer chains. Finally, the third degradation step is ascribed to the combustion of the carbonaceous residues [27,42].

a)

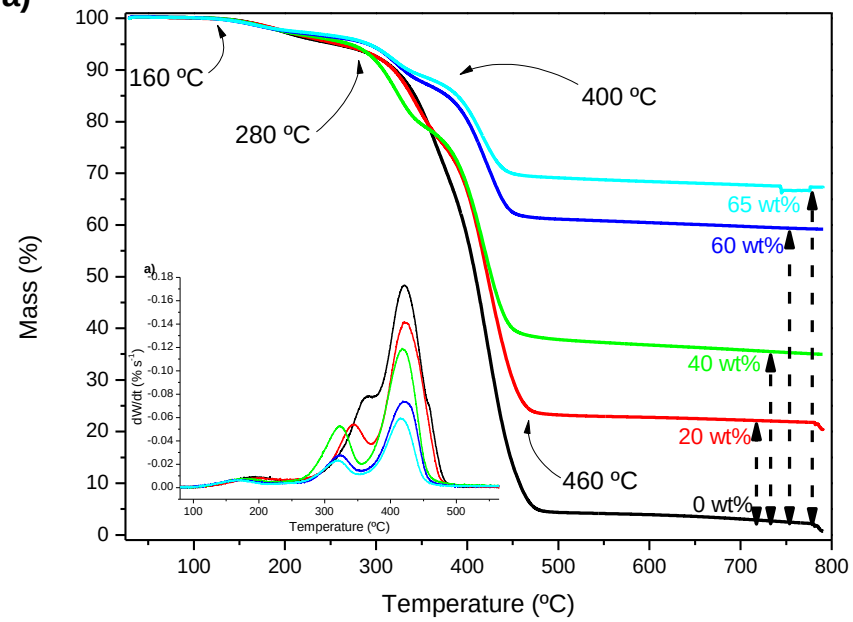
160 ºC
280 ºC
400 ºC
65 wt%
60 wt%
40 wt%
20 wt%
0 wt%
460 ºC
Mass (%)
Temperature (ºC)
a)
dW/dt (% s-1)
Temperature (ºC)

b)

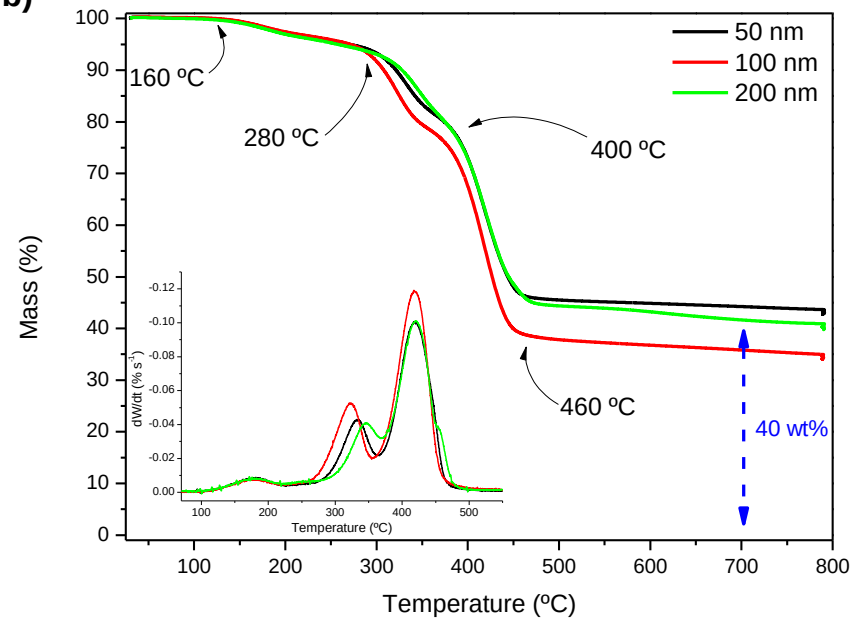
50 nm
100 nm
200 nm
160 ºC
280 ºC
400 ºC
460 ºC
40 wt%
Mass (%)
Temperature (ºC)
dW/dt (% s-1)
Temperature (ºC)

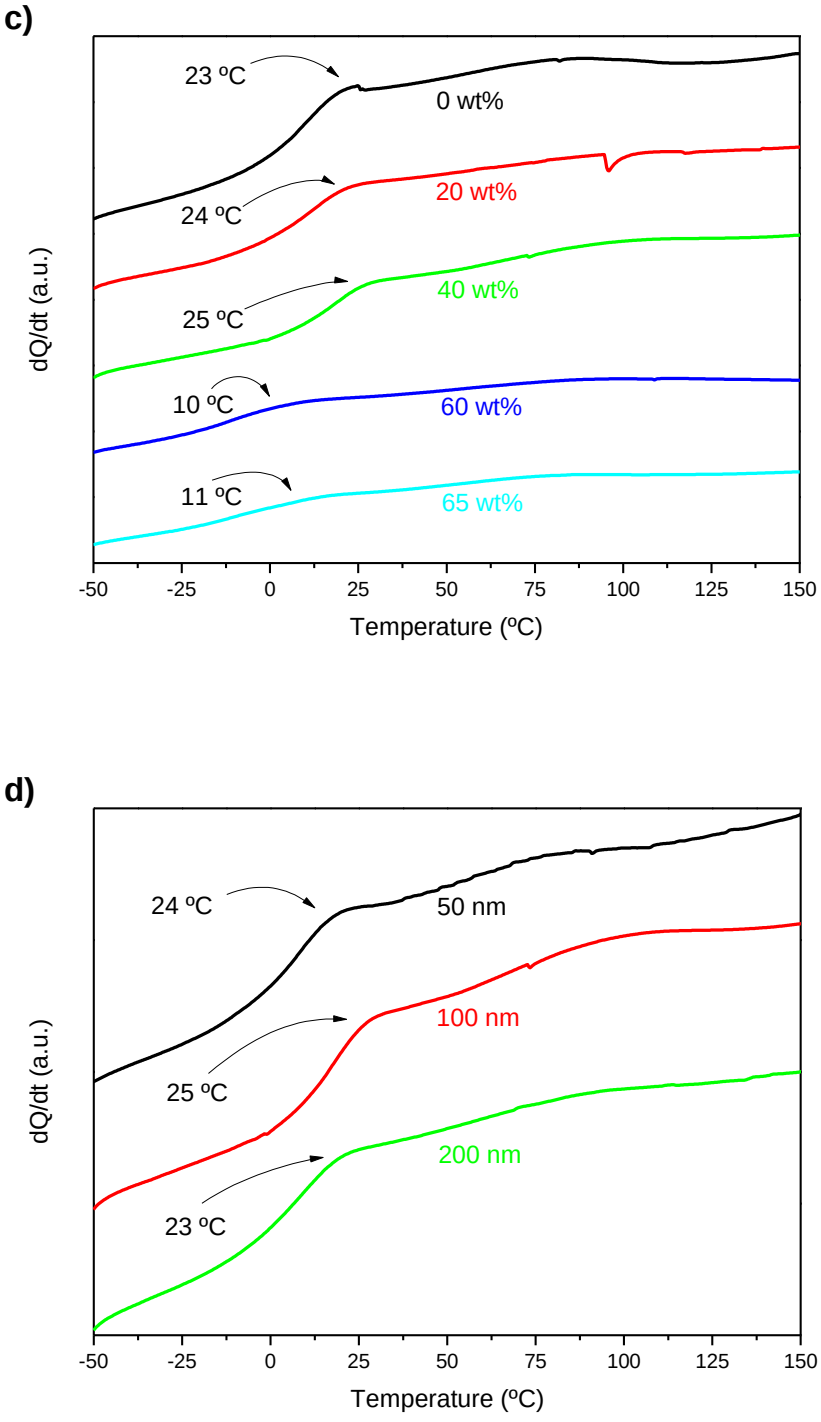

Figure 5 - Thermogravimetric (TG) and differential thermogravimetric (DTG) curves for neat PUA and the different $BaTiO_3$ composites with varying filler content (a) and size (b). Differential scanning calorimetry (DSC) thermograms in the first scan for neat PUA and the prepared composites with different $BaTiO_3$ content (c) and size (d).

Similar degradation profiles were obtained for composites independently of the filler content and size, being observed the same three differentiated degradation steps for all samples. On the other hand, the TG curves show that the degradation starts later when the filler content increases, denoting a slightly increase on the thermal stability of the PUA polymer. This

behaviour is larger for samples with higher filler contents and is attributed to the thermal insulator behaviour as well as barrier effect of the barium titanate, which influences the thermo-oxidative process of the PUA polymer [27]. This fact is reinforced by the fact that $BaTiO_3$ does not suffer degradation in the temperature range studied and the residual solid is in good agreement with the amount of ceramic filler loaded in each sample. Finally, there is not relevant influence of the barium titanate nanoparticle size on the thermal stability.

DSC thermograms of neat PUA and the $BaTiO_3$/PUA composites (Figure 5c and 5d) demonstrate that all samples exhibit similar thermal behaviour characterized by a glass transition that in neat polymer is around room temperature (23 ºC). The incorporation of ceramic particles into the photoresin slightly decreased the T_g of the PUA, being this decrease larger for increasing barium titanate content, being 23 ºC for the PUA0 sample and 11 ºC for PUA65_100 sample.

As previously indicated, the presence of nanofillers into the curable material affects the photopolymerization process mainly due to the absorption of UV light by the ceramic material. This produces a decrease on the light absorption by the photoinitiator and therefore, the effectiveness of the curing process is affected. Thus, the acrylic double bond conversion is reduced when the barium titanate content increases, leading to a flexibilization or plasticizing effect. This effect induces a lower crosslink density and a larger free volume within the polymer which results in a lower T_g [27]. As in the thermal stability results, barium titanate nanoparticle size has not influence on the T_g of the composites.

Mechanical characterization

UV-curable acrylate materials are limited for some applications due to their low strength and poor resistance to high temperature. However, thermal and mechanical properties can be tuned by adding nanofillers such as graphene, carbon nanotubes o ceramic particles [43,44]. In this study, the effect of barium titanate nanofillers on the mechanical properties of the composites has been addressed (Figure 6). The secant modulus (E), maximum stress (σ_b) and strain at brake (ε_b) were obtained by evaluating the results of uniaxial tensile tests of the samples. Figure 6a shows the representative stress-strain curves for PUA and the corresponding composites. Figure 6b and 6c show the evolution of the main mechanical parameters as a function of $BaTiO_3$ concentration and sizes, respectively. Table 2 summarizes the corresponding values of the mechanical properties.

Table 2 - Main mechanical parameters obtained from the tensile test for the prepared nanocomposites. E: Initial modulus; σ_b: stress at yield; ε_b: elongation at yield; $E_{Halpin\text{-}Tsai}$: theoretical initial modulus predicted by the Halpin-Tsai model [45].

Sample	E (MPa)	σ_b (MPa)	ε_b (%)	$E_{Halpin\text{-}Tsai}$ (MPa)
PUA0	5.8 ± 0.1	2.1 ± 0.2	40.4 ± 3.5	5.8
PUA20_100	6.9 ± 0.3	2.6 ± 0.2	37.9 ± 1.9	7.0
PUA40_50	10.2 ± 0.4	2.6 ± 0.2	31.7 ± 3.0	-
PUA40_100	8.5 ± 0.6	3.3 ± 0.7	37.2 ± 4.2	8.9
PUA40_200	8.6 ± 0.5	3.7 ± 0.5	39.0 ± 4.1	-
PUA60_100	21.0 ± 0.2	4.3 ± 0.2	23.8 ± 1.5	12.7
PUA65_100	27.8 ± 1.1	5.4 ± 0.3	25.3 ± 1.5	14.4

Neat UV cured PUA polymer shows a mechanical behaviour [46] characterized by a secant modulus E of 5.8 ± 0.1 MPa and strain at brake ε_b of 40.4 ± 3.5. The addition of $BaTiO_3$ nanoparticles produces an increase of the initial modulus up to 27.8 ± 1.1 for the sample PUA65_100, together with a corresponding decrease of the maximum strain from 40.1 ± 3.5 to 25.3 ± 1.5. Thus, it is demonstrated that the inclusion of barium titanate [47] act as mechanical reinforcement due to the high tensile modulus of the inorganic component compared to the organic one, as well as due to the good wettability between filler and matrix. It is observed that the larger agglomerates observed for samples PUA60_100 and PUA65_100 cause a decrease on the maximum elongation, as those act as breaking points on the polymer matrix due to stress accumulation [48]. It is worth noting that the secant modulus increases exponentially with ceramic particles content (Figure 6b), which is explained by the fact that the internal network created by the ceramic filler, that is responsible for the reinforcement effect, has been formed when the content of $BaTiO_3$ within the polymer matrix is larger than 50 wt% [46].

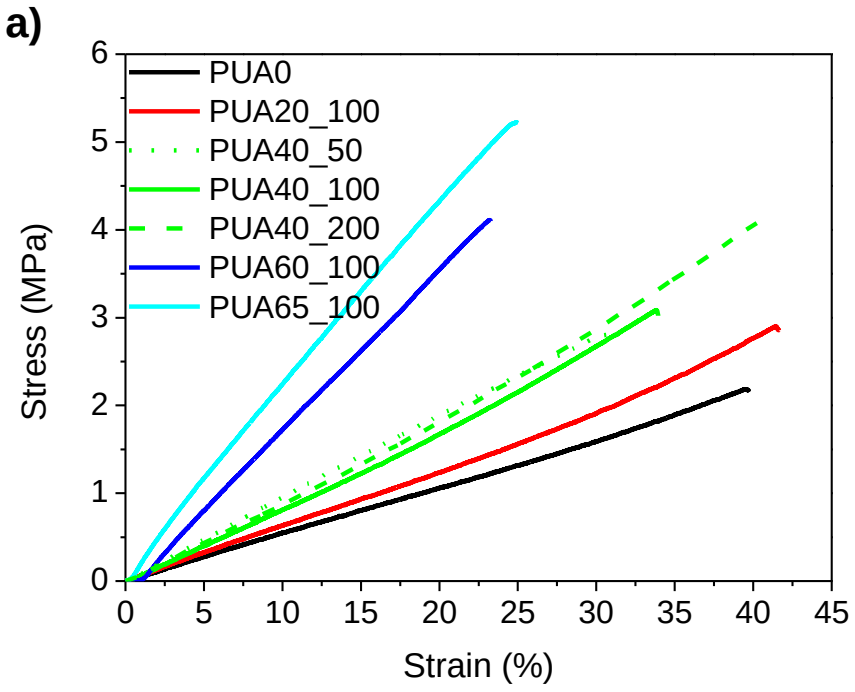
a)
PUA0
PUA20_100
PUA40_50
PUA40_100
PUA40_200
PUA60_100
PUA65_100
Stress (MPa)
Strain (%)
0
1
2
3
4
5
6
0
5
10
15
20
25
30
35
40
45

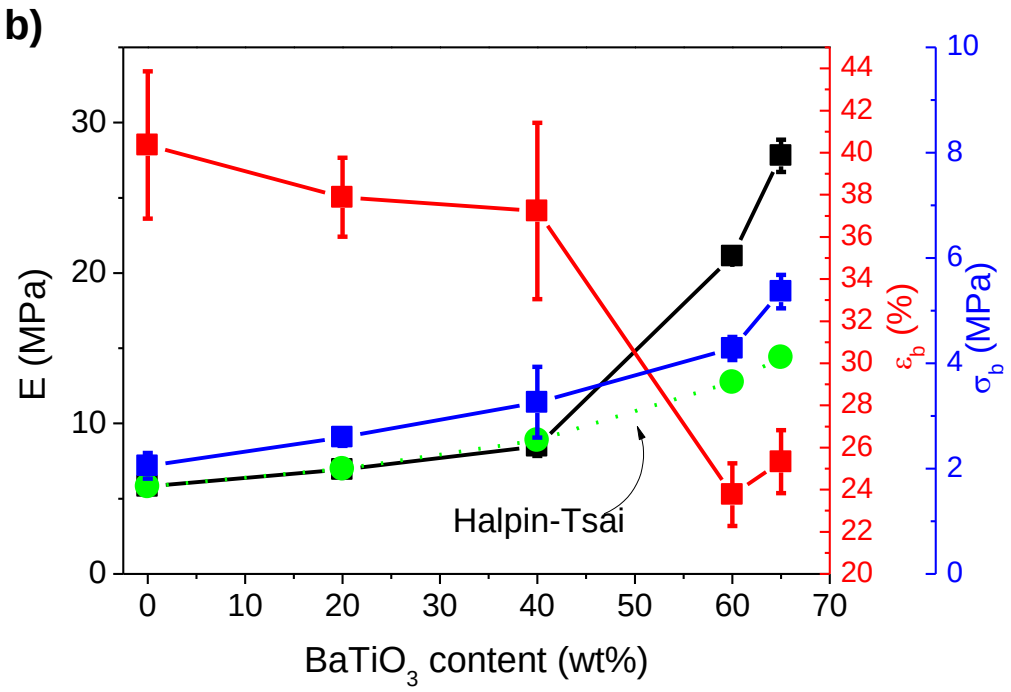
b)
E (MPa)
ε_b (%)
σ_b (MPa)
Halpin-Tsai
$BaTiO_3$ content (wt%)
0
10
20
30
0
10
20
30
40
50
60
70
20
22
24
26
28
30
32
34
36
38
40
42
44
0
2
4
6
8
10

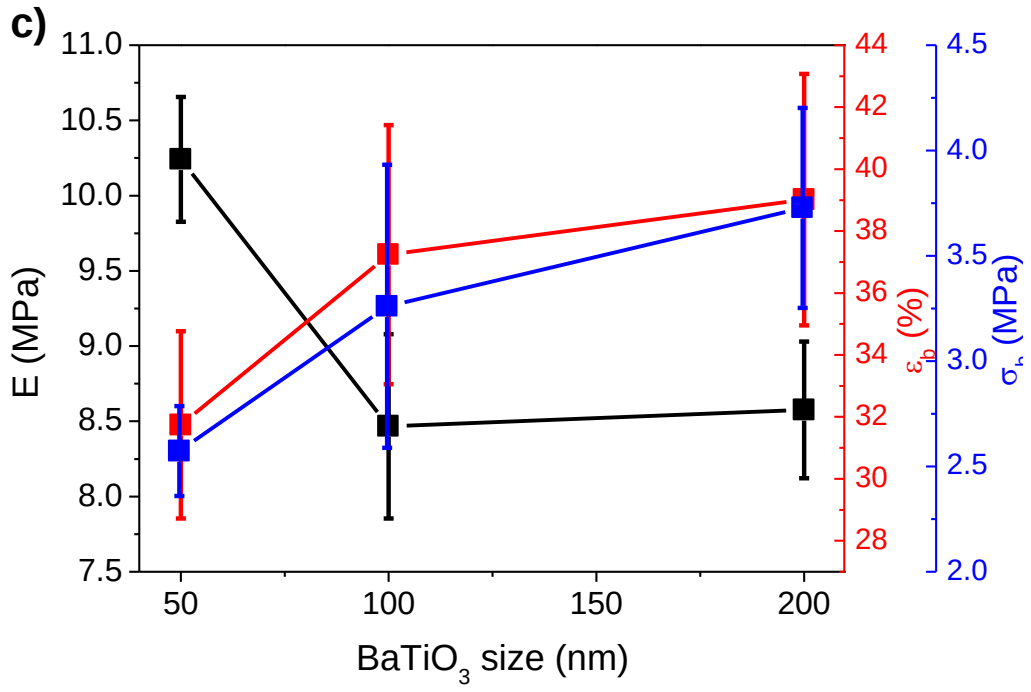

Figure 6 - Representative stress−strain curves for neat PUA and the corresponding composites (a), experimental data and fitting results of neat PUA and the prepared composites with different amounts of $BaTiO_3$ nanoparticles determined according to the modified Halpin−Tsai model (b) and experimental results for neat PUA and the prepared composites with different $BaTiO_3$ nanoparticles sizes.

Comparing samples with different nanoparticle sizes, the same tensile behaviour is observed for samples PUA40_50, PUA40_100 and PUA40_200, showing that the nanoparticles reinforce effect of the polymer matrix occurs for the three filler sizes. However, attending to the mechanical parameters (Figure 6c), a slight difference is observed for the three particle sizes. The tensile modulus decreases from 10.2 ± 0.4 MPa for the same sample with smallest particle size to 8.6 ± 0.5 MPa for the sample that contains 200 nm $BaTiO_3$ nanoparticles. In the case of σ_b and ε_b, a slight increas is observed between 2.6 ± 0.2 to 3.7 ± 0.5 and between 31.7 ± 3.0 to 39.0 ± 4.1, respectively, for the same samples. These results are explained in terms of the surface area interaction between the fillers and the polymer. Thus, small agglomerates in the samples with smallest particle size can actuate as breaking points and despite the inorganic matrix reinforce of the PUA polymer (higher E), the composite becomes more fragile, leading to an early break (lower σ_b and ε_b). Similar results were observed by Capsal *et al.* with polyamide 11/Barium titanate ferroelectric composites [48].

The experimentally obtained results for samples with 100 nm $BaTiO_3$ nanoparticles were compared with the theoretical predictions of the Halpin-Tsai model [45]:

$$\frac{E_c}{E_m} = \left(\frac{3}{8}\right)\left(\frac{1 + 2\rho\eta_L V_{BaTiO_3}}{1 - \eta_L V_{BaTiO_3}}\right) + \left(\frac{5}{8}\right)\left(\frac{1 + 2\eta_T V_{BaTiO_3}}{1 - \eta_T V_{BaTiO_3}}\right) \quad (3)$$

$$\eta_L = \frac{E_r - 1}{E_r + 2\rho} \; ; \; \eta_T = \frac{E_r - 1}{E_r + 2}$$

where E_c and E_m are the initial modulus of the composite and matrix [49] respectively, ρ is the $BaTiO_3$ nanoparticles aspect ratio (set at 1, spherical), V_{BaTiO_3} is its volume fraction within the nanocomposite and E_R is defined as the ratio between the Young´s modulus of the filler and the matrix. The density of ceramic filler is obtained from the technical datasheet of the suppliers, being 5.85 g cm^{-3}, and the density of PUA polymer is 1.55 g cm^{-3}.

Figure 6b shows that the experimental values can be markedly well described by the model for $BaTiO_3$ nanoparticles contents up to 40 wt% and remain above the theoretical predictions for higher ceramic particles contents. Those results indicate that the Hapin Tsai model properly describes the experimental results until the formation of large agglomerates (see Figure 3g and h) that affect the mechanical properties [45].

Dielectric properties

The dielectric constant or relative permittivity (ε´) and the dielectric losses (tan δ) as a function of the frequency are among the most relevant parameter on this types of composites [33]. In this sense, Figure 7a shows the frequency dependence of the room temperature dielectric constant for neat PUA and the different $BaTiO_3$/PUA composites, and Figure 7b and c show the relative permittivity measured and the corresponding losess at 1 kHz for the same samples, whereas Figure 7d shows that dielectric constant as a function of filler size.

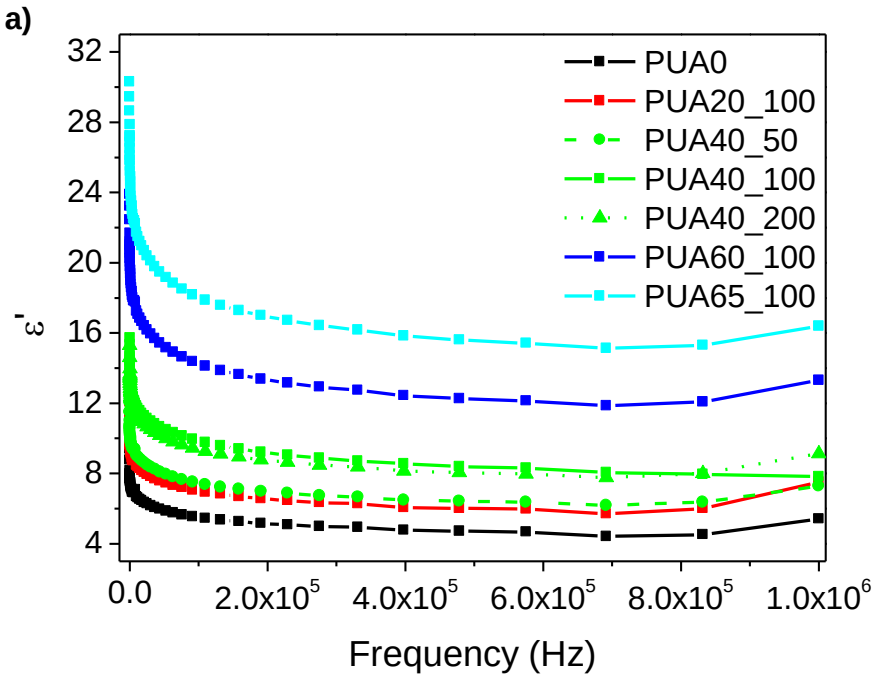

b)

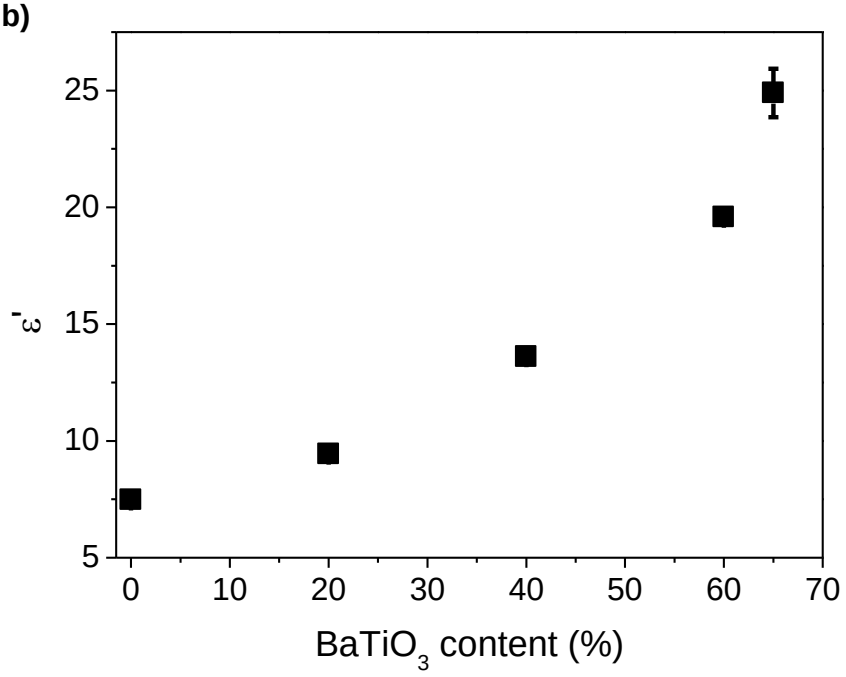
25
20
15
10
5
ε'
0
10
20
30
40
50
60
70
BaTiO3 content (%)

c)

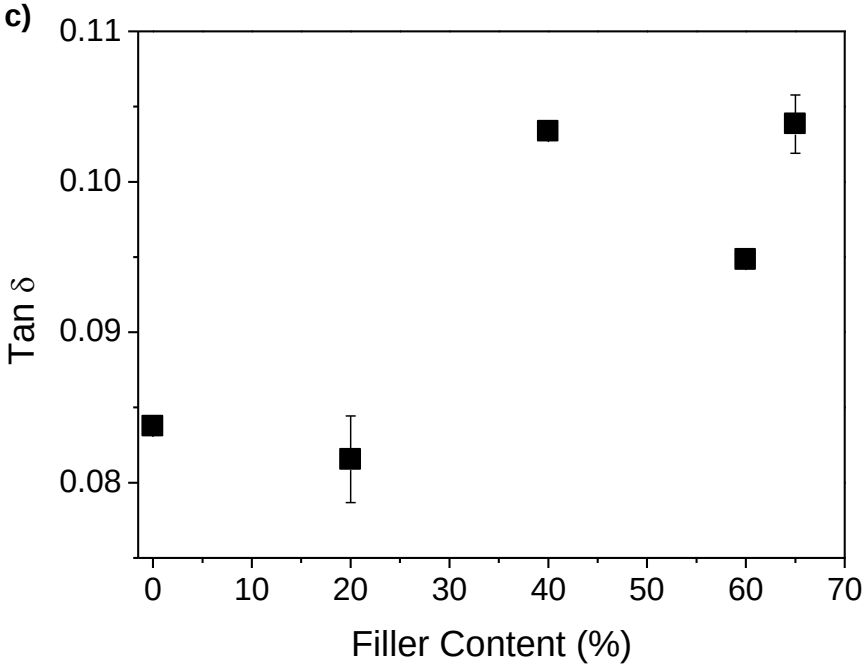
0.11
0.10
0.09
0.08
Tan δ
0
10
20
30
40
50
60
70
Filler Content (%)

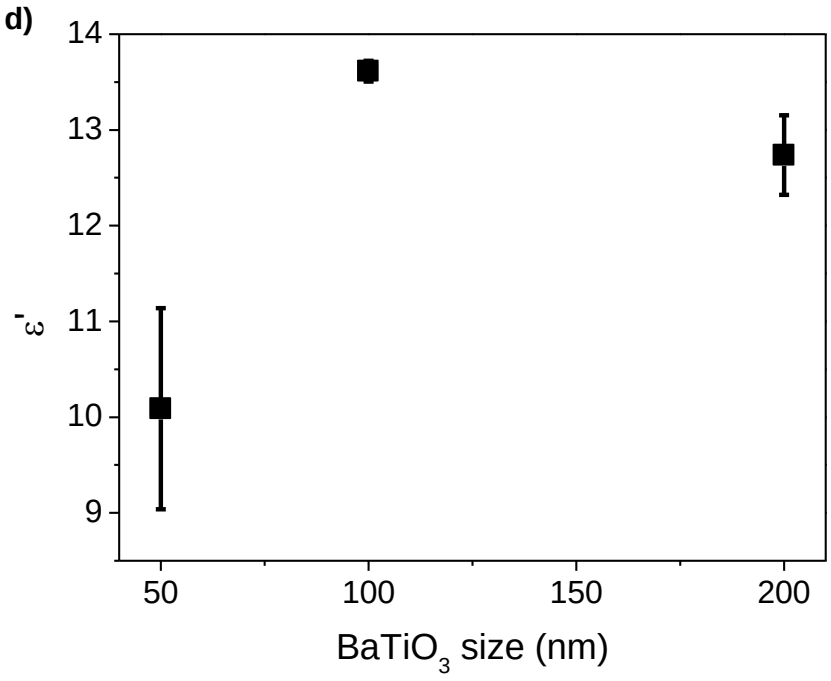
d)
14
13
12
11
10
9
ε'
50
100
150
200
BaTiO3 size (nm)

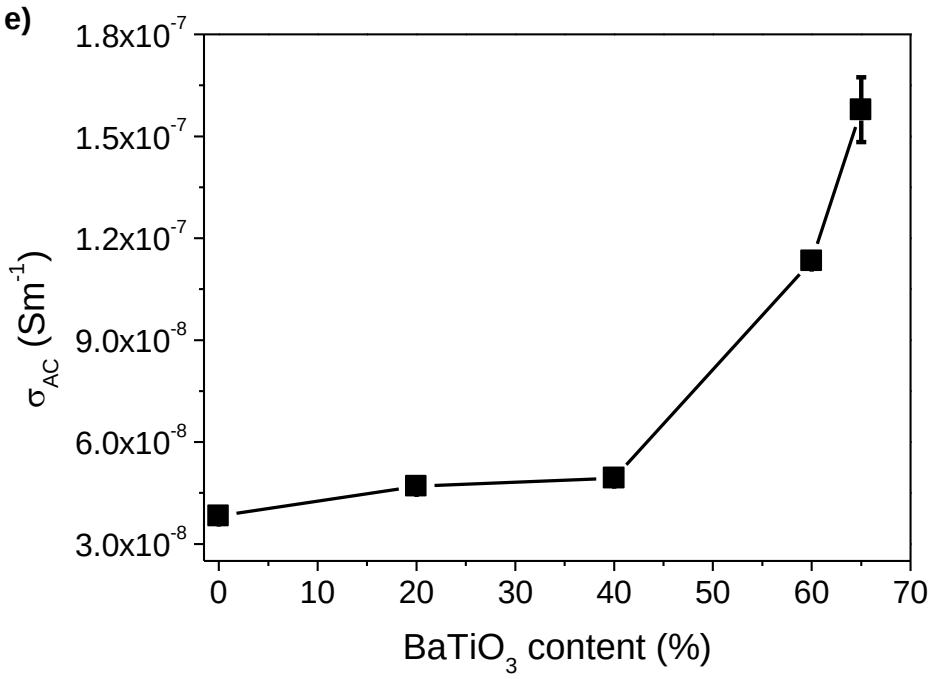
e)
1.8x10-7
1.5x10-7
1.2x10-7
9.0x10-8
6.0x10-8
3.0x10-8
σAC (Sm-1)
0
10
20
30
40
50
60
70
BaTiO3 content (%)

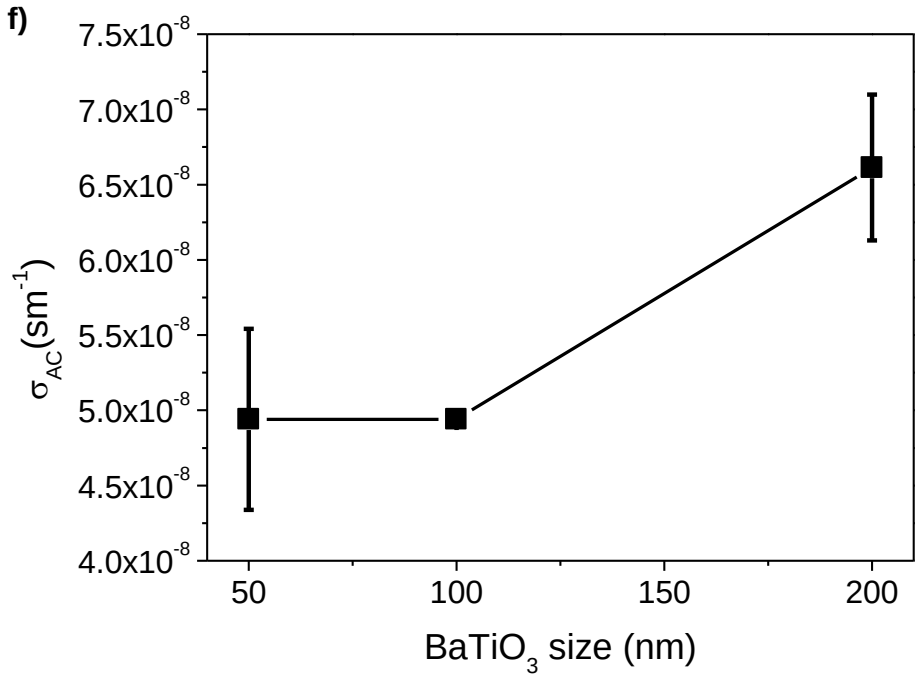

Figure 7 – (a) Relative permittivity as a function of frequency at room temperature for neat PUA and all prepared composites. Relative permittivity (b) and the tan δ dielectric loss values (c) at 1KHz at room temperature as a function of $BaTiO_3$ content. Relative permittivity at 1 kHz at room temperature as a function $BaTiO_3$ nanoparticles size (d). Electrical conductivity at room temperature and 1 kHz of the neat PUA and the prepared composites as a function of filler content for 100 nm nanoparticles (e) and filler size (f).

It is shown that ε' decreased with the frequency for all samples, independently of the filler size or content. This behaviour is attributed to the dipolar relaxation with increasing frequency as well as to interfacial polarization effects. The titanium ions of the $BaTiO_3$ structure occupy a position that is too large for that ion. Thus, when a field is applied, the positively charged ion (Ti^{4+}) can move in the direction of the negative pole easily over a small distance creating a very large polarization and thereby increasing the dielectric constant or relative permittivity of the material. When the field is removed, the ion is reoriented. At large frequencies, the titanium ion does not have enough time to reorient itself in the structure giving rise to the relaxation of the dipoles, which is accompanied with the corresponding variations in the dielectric losses [50,51].

Relative permittivity measured at 1 kHz increases as a function of filler content increase (Figure 7c) from 7.48 ± 0.08 for neat polymer up to 13.61 ± 0.11 for the PUA40_100 sample. The maximum relative permittivity value was achieved for the maximum concentration of $BaTiO_3$ nanoparticles in sample PUA65_100 that shows and ε' of 24.90 ± 1.04. Further, the relative permittivity measured at 1 kHz as a function of filler size shows that an increase on the filler size allows a slightly increase on the ε'. Thus, the PUA40_50 sample shows a dielectric constant of 10.09 ± 1.05 and PUA40_200 sample of 12.74 ± 0.41. Figure 7d shows that the dielectric constant reaches a nearly constant value, which is explained in terms of agglomeration of the smallest $BaTiO_3$ nanoparticles that induces a similar electrical behaviour than the 100 nm

and 200 nm particles [27]. Similar values and behaviours were found in the literature for several polymer/ceramic particle composites [27,33,52–54], but with slightly differences based on the different polymer matrix and the interaction of the polymer and the ceramic particles. Thus, a study of this interaction was evaluated.

In addition, the dependence of the electrical conductivity (σ) (obtained at 1 kHz) with the $BaTiO_3$ nanoparticle concentration and size was obtained using the equation (4) [45]:

$$\sigma = 2\pi f \varepsilon_0 \varepsilon'' \quad (4)$$

where f is the frequency in Hz, ε_0 represents the vacuum permittivity (8.854×10^{-12} F·m^{-1}) and ε′′ is the imaginary part of the permittivity represented as $\varepsilon'' = \varepsilon' \cdot \tan\delta$. The results obtained are represented in Figure 7e and 7f.

All prepared composites can be considered as insulating materials due to their low σ values (in order of 10^{-8} S·m^{-1}), in particular, the neat PUA matrix with a value of conductivity about 3.82 x 10^{-8} S·m^{-1}. Similar to dielectric properties, the a.c. conductivity increases with increasing ceramic content being 4.94 x 10^{-8} S·m^{-1} for PUA40_100 sample and reaching the highest value of conductivity (1.58 x 10^{-7} S·m^{-1}) for the sample with higher $BaTiO_3$ content. These slightly but pronounced increase on the conductivity upon $BaTiO_3$ addition is associated with the increase of interfacial charges and is related to Maxwell-Wargner-Sillars effects [50,51].

In the case of size dependence, a slight increase of the a.c. electrical conductivity is observed when the barium titanate nanoparticle size increases. Nevertheless, this increase is lower than 1 order of magnitude and the maximum conductivity obtained for PUA40_200 sample is 6.61 x 10^{-8} S·m^{-1}.

Theoretical evaluation of the dielectric properties

The theoretical models for the analysis of the dielectric constant allow to evaluate the nature of the interactions between the matrix and the fillers, responsible for the dielectric response of the composites. The $BaTiO_3$/PUA composites have been analyzed, considering the nanoparticles size (Φ=100 nm) and concentration (20 wt%, 40 wt%, 60 wt% and 65wt% corresponding to volume fractions of 0.06212, 0.15012, 0.28440 and 0.32979, respectively). The most appropriate models considering filler size and concentration will be presented and discussed.

The differences between models are related to differences in the considerations of the relevant interactions between the polymeric matrix and the fillers, as well as on the relevance of the effect of filler volume fraction. Although the different models consider different interactions, all of them predict the increase of the dielectric constant with increasing filler content. The most simple models include Maxwell-Garnett (equation-(5)) and Furukawa (equation-(7)), typically

used to experimentally explain the dielectric behavior of the composites [55,56], but being unable to predict the experimental results for higher fillers contents, as they do not consider filler shape and size, which are needed to better understand the interactions and aggregation effects of the fillers [26,56], for example.

The models of Maxwell-Garnett [57,58] and Furukawa [59] consider the incorporation of spherical fillers into a polymeric matrix with no interactions between particles and between matrix and particles, also without considering filler size effects.
The Maxwell-Garnet model is represented by:

$$\varepsilon = \varepsilon_1 \left(1 + \frac{3\nu_2\gamma}{1-\nu_2\gamma}\right) \tag{5}$$

where

$$\gamma = \frac{\varepsilon_2 - \varepsilon_1}{\varepsilon_2 + 2\varepsilon_1} \tag{6}$$

and ε represents the dielectric constant, ν is the volume fraction and the subscripts 1 and 2 represent the matrix and filler, respectively. T. Furukawa, K. Ishida, et al. [59] proposed an approximation in the Rayleigh model, considering that the dielectric constant of the fillers is usually much higher than the matrix ($\varepsilon_2 \gg \varepsilon_1$), so that the behavior of the dielectric constant with filler content is represented by:

$$\varepsilon = \varepsilon_1 \frac{1 + 2\nu_2}{1 - \nu_2} \tag{7}$$

Later, models were developed considering also spherical dielectric inclusions into a polymeric matrix but considering also the materials polarization due to the applied electric field, the variation in local field and interactions between the fillers and the local and applied field [26]. When an electric field is applied to a composite material, the dielectric particles can be, in a good approximation, considered as electric dipoles changing the electric field in its surroundings. This effect can be neglected for low filler concentrations, however for higher concentrations the interaction between particles cannot be ignored [60]. Thus, Bruggeman established a symmetrical expression considering this phenomenon [57]:

$$\nu_1 \frac{\varepsilon_1 - \varepsilon}{\varepsilon_1 + (d-1)\varepsilon} + \nu_2 \frac{\varepsilon_2 - \varepsilon}{\varepsilon_2 + (d-1)\varepsilon} = 0 \tag{8}$$

where *d* is the dimensionality of the system. An improvement of the Maxwell-Garnett model considering also the interactions between fillers, lead to rewrite equation (5) as [58]:

$$\varepsilon = \varepsilon_1 \left[1 + \frac{3\nu_2\gamma}{1 - \nu_2\gamma - \frac{2}{3}\nu_2\gamma \ln\left(\frac{8+\gamma}{8-2\gamma}\right)}\right] \tag{9}$$

where γ is defined by equation (6).

Most precise and complex models also introduce the effects of the shape and relative orientation of the fillers, considering in most of the cases an ellipsoids shape for the fillers. This information appears in the equations as depolarization factor (*n*) or shape parameter (*n'*). Most precisely, the *n* factor is influenced by the principal axe's length of the fillers and the relative orientation to the applied filed [61]. An extension of the Sillars's work, led to van Beek to present the following equation, taking in consideration the factor *n* [62]:

$$\varepsilon = \varepsilon_1 \frac{\varepsilon_1 + [n(1-\nu_2)+\nu_2](\varepsilon_2-\varepsilon_1)}{\varepsilon_1 + n(1-\nu_2)(\varepsilon_2-\varepsilon_1)} \quad (10)$$

In particular, for composite samples with only one filler type, W. R. Tinga, W. A. G. Voss, et al. [63] proposed the expression:

$$\frac{\varepsilon-\varepsilon_1}{\varepsilon_1} = \nu_2 \frac{\varepsilon_2-\varepsilon_1}{\varepsilon_1 + n_2(\varepsilon_2-\varepsilon_1) - n_1\nu_2(\varepsilon_2-\varepsilon_1)} \quad (11)$$

For models that introduce the *n'* factor, T. Yamada, T. Ueda, et al. [64] deduced an equation for an ellipsoidal particle dispersion

$$\varepsilon = \varepsilon_1 \left[1 + \frac{n'\nu_2(\varepsilon_2-\varepsilon_1)}{n'\varepsilon_1 + (\varepsilon_2-\varepsilon_1)(1-\nu_2)}\right] \quad (12)$$

Taking the same considerations, Wiener proposed the following equation [65]:

$$\frac{\varepsilon-1}{\varepsilon+n'} = \frac{\nu_2(\varepsilon_2-\varepsilon_1)}{\varepsilon_2+n'} + \frac{(1-\nu_2)(\varepsilon_1-1)}{\varepsilon_1+n'} \quad (13)$$

Simulations of the different models, described through equations (5) to (13) allow to model the dielectric behavior of composites samples and are represented in Figure 8 as a function of filler volume fraction, considering $\varepsilon_1 = 7.48$ (measured) for the polymer matrix and $\varepsilon_2 = 150$ [66] for the $BaTiO_3$ filler. The volume fraction change between 0 and 1 and the experimental data are also represented.

XXXXX

The prediction of the dielectric constant given by the Bruggeman model is represented for each value of *d*. In the case of d=1, the Bruggeman model has the worst prediction for the dielectric constant. The Maxwell-Garnett, Maxwell-Garnett 2 (taking into account the interactions between fillers and the applied field), Furukawa and Bruggeman (d=2) models show the same behavior for low filler concentrations ($\nu_2 < 0.2$) suggesting that, in this regime, the composite permittivity is almost independent from the filler permittivity. For higher volume fraction, the models start to show relevant differences one another. Increasing volume fraction leads to an increase of the dielectric constant of the composite until $\nu_2 = 1$, excepting for the Maxwell-Garnett model 2 which shows a vertical asymptote for $\nu_2 \approx 0.95$. Although Maxwell-Garnett 2 model takes into consideration interactions between fillers and the applied field, there is just a slight difference between the two author's models.

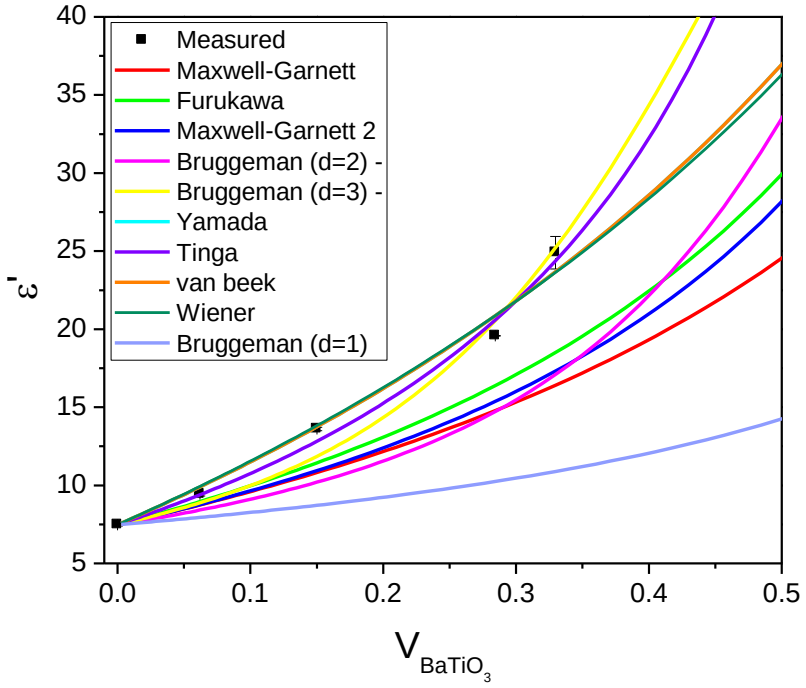

Figure 8 - Theoretical models and experimental results for a $BaTiO_3$/PUA composites of 100 nm diameter particles. The experimental results correspond to a frequency of 1kHz.

The Maxwell-Garnett, Maxwell-Garnett 2, Furukawa and Bruggeman (d=2) models predict the same behavior for $v_2 = 0\ (\varepsilon = \varepsilon_1)$ and in the regime limit of $v_2 = 1$ the Maxwell-Garnett and Bruggeman (d=2) models predict a dielectric constant of $\varepsilon = \varepsilon_2$. In the case of the Furukawa model, ε goes to infinite. For these models, the Bruggeman's model (d=2) predict the higher dielectric constant for $v_2 > 0.4$.

The experimental-theoretical difference was calculated as relative percentage deviation - $\langle \delta_r \rangle$, for Maxwell-Garnett, Furukawa, Maxwell-Garnett 2, Bruggeman (for d=1,2 and 3) models through equation (14)

$$\langle \delta_r \rangle = \frac{|\varepsilon_{exp} - \varepsilon_{mod}|}{\varepsilon_{exp}} \times 100\ \% \qquad (14)$$

where ε_{exp} is the experimental data measured and ε_{mod} the predicted dielectric constant for the corresponding model. The results are summarized in Table 3. All these models show deviations less than 12% for $v_2 = 0.06212$ (except Bruggeman (d=1)) but with increasing filler contents, the models that not considered the filler agglomeration effects (Maxwell-Garnett and Furukawa), are unable of predict the experimental data. This means that the interactions only become important for a certain volume fraction. Even though the models of Maxwell-Garnett 2 and Bruggeman (d=2) consider the interaction between nanoparticles and the field, they are unable to properly model the experimental data. Within these models, the Furukawa model is

the one with better predictions. Only the Bruggeman (d=3) model can describe the data for all ν_2 with deviations less than 13%. This deviation values are related to the agglomerations affect that occurs for higher volume fraction leading to the break of homogeneity condition underlaying all models [26]. Further, the high surface area due to the filler size (Φ=100 nm), leading to an increase of the space charge distribution and Maxwell-Wagner-Sillars contributions to the dielectric behavior [33], can also account for these deviations.

Table 3 – Relative percentage deviation for the theoretical models for each volume fraction.

	Relative percentage deviation - $\langle\delta_r\rangle$ (%)			
Models\ Volume faction (ν_2)	**0.06212**	**0.15012**	**0.28440**	**0.32979**
Maxwell-Garnett	7	21	24	34
Furukawa	5	16	16	26
Maxwell-Garnett 2	7	20	21	30
Bruggeman (d=1)	16	36	48	56
Bruggeman (d=2)	11	25	25	31
Bruggeman (d=3)	6	13	5	1

For the remaining models (van Beek, Tinga, Yamada and Wiener), the experimental data were fitted to determine the depolarization factor *n* or shape parameter *n′*, for the corresponding models, by computational iteration. These models predict in a more precise way the dielectric behavior of the composite showing the important contributions of the filler's shape and orientation. The obtained results are summarized in Table 4 showing the *n* and *n′* values and the respective R-square for the fitting procedure.

Table 4 – The parameters *n* and *n′* for the respective models obtained by computational iteration by fitting the experimental data.

	Models			
	Yamada	**Wiener**	**Tinga**	**van Beek**
n_1	--	--	0.357 ± 0.145	0.149 ± 0.009
n_2	--	--	0.211 ± 0.046	--
n′	6.724 ± 0.419	48.167 ± 3.634	--	--
R-Square	0.98397	0.98286	0.99071	0.98397

Although the Tinga model shows a vertical asymptote for $\nu_2 \approx 0.74$, when it was compared the R-Square values, all these models have a good fitting to the experimental data, with a more precise prediction for the Tinga model, followed by the Yamada, van Beek and Wiener models. The difference between the obtained factors is due to the physical principles considered by the

models. The value *n′* can mean the ratio between ellipsoidal axis but also the size of agglomeration and homogeneity of the sample.

Thus, it can be concluded that the model that better predict the behavior of the $BaTiO_3$/PUA composites is the Tinga model and therefore, the relevant interactions, together with the filler and matrix dielectric constant and filler concentrations are the materials polarization due to the applied electric field, the variation in local field and interactions between the fillers and the local and applied field and the influence of the principal axe′s length of the fillers and the relative orientation to the applied field. So, the equation (11), that is a special case of the Tinga model that describes a ellipsoidal inclusion of two phases, must be considered to properly tailor and understating composite dielectric response.

Conclusion

UV curable barium titanate/polyurethane acrylate ($BaTiO_3$/PUA) composites are presented with varying ceramic contents, allowing to obtain dielectric materials with tailored dielectric response for electronic applications, among others. PUA composites with $BaTiO_3$ filler contents up to 65 wt% for filler sizes between 50 nm and 200 nm have been evaluated. A good dispersion stability up to 160 ºC and mechanical flexibility. Further, the dielectric constant can be as high as 25 for the samples with the highest filler content, independently of the filler size, the dielectric response as a function of filler concentration being suitably described by the Tinga model for the dielectric behavior of composites.

Acknowledgements

Financial support from the Basque Government under the ELKARTEK, HAZITEK and PIBA (PIBA-2018-06) programs is acknowledged. We acknowledge the receipt of funding from the European Union`s Horizon 2020 Programme for Research, ICT-02-2018 – Flexible and Wearable Electronics, Grant agreement no. 824339 – WEARPLEX. The authors also thank the Portuguese Foundation for Science and Technology (FCT) in the frameworks of the Strategic Project PEST-C/FIS/UI607/2019 and the SFRH/BD/140242/2018 grant (T.R.M.). Technical and human support provided by SGIker (UPV/EHU, MICINN, GV/EJ, EGEF and ESF) is gratefully acknowledged.

References

[1] Y. Lu, Industry 4.0: A survey on technologies, applications and open research issues, J. Ind. Inf. Integr. 6 (2017) 1–10. doi:10.1016/j.jii.2017.04.005.

[2] V. Roblek, M. Meško, A. Krapež, A Complex View of Industry 4.0, SAGE Open. 6 (2016). doi:10.1177/2158244016653987.

[3] I. Lee, K. Lee, The Internet of Things (IoT): Applications, investments, and challenges for enterprises, Bus. Horiz. 58 (2015) 431–440. doi:10.1016/j.bushor.2015.03.008.

[4] P.P. Ray, A survey on Internet of Things architectures, J. King Saud Univ. - Comput. Inf. Sci. 30 (2018) 291–319. doi:10.1016/j.jksuci.2016.10.003.

[5] A. Zanella, N. Bui, A. Castellani, L. Vangelista, M. Zorzi, Internet of things for smart cities, IEEE Internet Things J. 1 (2014) 22–32. doi:10.1109/JIOT.2014.2306328.

[6] J. Gubbi, R. Buyya, S. Marusic, M. Palaniswami, Internet of Things (IoT): A vision, architectural elements, and future directions, Futur. Gener. Comput. Syst. 29 (2013) 1645–1660. doi:10.1016/j.future.2013.01.010.

[7] C. Mendes-Felipe, J. Oliveira, I. Etxebarria, J.L. Vilas-Vilela, S. Lanceros-Mendez, State-of-the-Art and Future Challenges of UV Curable Polymer-Based Smart Materials for Printing Technologies, Adv. Mater. Technol. 4 (2019) 1–16. doi:10.1002/admt.201800618.

[8] J. Oliveira, V. Correia, H. Castro, P. Martins, S. Lanceros-Mendez, Polymer-based smart materials by printing technologies: Improving application and integration, Addit. Manuf. 21 (2018) 269–283. doi:10.1016/j.addma.2018.03.012.

[9] J. Oliveira, R. Brito-Pereira, B.F. Gonçalves, I. Etxebarria, S. Lanceros-Mendez, Recent developments on printed photodetectors for large area and flexible applications, Org. Electron. Physics, Mater. Appl. 66 (2019) 216–226. doi:10.1016/j.orgel.2018.12.028.

[10] Y. Zhan, Y. Mei, L. Zheng, Materials capability and device performance in flexible electronics for the Internet of Things, J. Mater. Chem. C. 2 (2014) 1220–1232. doi:10.1039/c3tc31765j.

[11] M. Haras, T. Skotnicki, Thermoelectricity for IoT – A review, Nano Energy. 54 (2018) 461–476. doi:10.1016/j.nanoen.2018.10.013.

[12] K.N. Paracha, S.K. Abdul Rahim, P.J. Soh, M. Khalily, Wearable Antennas: A Review of Materials, Structures, and Innovative Features for Autonomous Communication and Sensing, IEEE Access. 7 (2019) 56694–56712. doi:10.1109/ACCESS.2019.2909146.

[13] F. Narita, M. Fox, A Review on Piezoelectric, Magnetostrictive, and Magnetoelectric Materials and Device Technologies for Energy Harvesting Applications, Adv. Eng. Mater. 20 (2018) 1–22. doi:10.1002/adem.201700743.

[14] Y. Bai, H. Jantunen, J. Juuti, Energy harvesting research: The road from single source to multisource, Adv. Mater. 30 (2018) 1–41. doi:10.1002/adma.201707271.

[15] M. Zhou, M.S.H. Al-Furjan, J. Zou, W. Liu, A review on heat and mechanical energy harvesting from human – Principles, prototypes and perspectives, Renew. Sustain. Energy Rev. 82 (2018) 3582–3609. doi:10.1016/j.rser.2017.10.102.

[16] S. Khan, L. Lorenzelli, R.S. Dahiya, Technologies for printing sensors and electronics over large flexible substrates: A review, IEEE Sens. J. 15 (2015) 3164–3185. doi:10.1109/JSEN.2014.2375203.

[17] K.K.B. Hon, L. Li, I.M. Hutchings, Direct writing technology-Advances and developments, CIRP Ann. - Manuf. Technol. 57 (2008) 601–620. doi:10.1016/j.cirp.2008.09.006.

[18] M. Gao, L. Li, Y. Song, Inkjet printing wearable electronic devices, J. Mater. Chem. C. 5 (2017) 2971–2993. doi:10.1039/c7tc00038c.

[19] A.H. Sirringhaus, T. Kawase, R.H. Friend, T. Shimoda, M. Inbasekaran, W. Wu, E.P. Woo, High-Resolution Inkjet Printing of All-Polymer Transistor Circuits Published by : American Association for the Advancement of Science Stable URL : http://www.jstor.org/stable/3081605 High-Resolution Inkjet Printing of ALL-Polymer Transistor Circuits, 290 (2016) 2123–2126.

[20] Z.P. Yin, Y.A. Huang, N.B. Bu, X.M. Wang, Y.L. Xiong, Inkjet printing for flexible electronics: Materials, processes and equipments, Chinese Sci. Bull. 55 (2010) 3383–3407. doi:10.1007/s11434-010-3251-y.

[21] A. Rida, L. Yang, R. Vyas, M.M. Tentzeris, Conductive inkjet-printed antennas on flexible low-cost paper-based substrates for RFID and WSN applications, IEEE Antennas Propag. Mag. 51 (2009) 13–23. doi:10.1109/MAP.2009.5251188.

[22] K. Kordás, T. Mustonen, G. Tóth, H. Jantunen, M. Lajunen, C. Soldano, S. Talapatra, S. Kar, R. Vajtai, P.M. Ajayan, Inkjet printing of electrically conductive patterns of carbon nanotubes, Small. 2 (2006) 1021–1025. doi:10.1002/smll.200600061.

[23] A. Kamyshny, S. Magdassi, Conductive nanomaterials for printed electronics, Small. 10 (2014) 3515–3535. doi:10.1002/smll.201303000.

[24] F. Torrisi, T. Hasan, W. Wu, Z. Sun, A. Lombardo, T.S. Kulmala, G.W. Hsieh, S. Jung, F. Bonaccorso, P.J. Paul, D. Chu, A.C. Ferrari, Inkjet-printed graphene electronics, ACS Nano. 6 (2012) 2992–3006. doi:10.1021/nn2044609.

[25] V. Correia, K.Y. Mitra, H. Castro, J.G. Rocha, E. Sowade, R.R. Baumann, S. Lanceros-Mendez, Design and fabrication of multilayer inkjet-printed passive components for printed electronics circuit development, J. Manuf. Process. 31 (2018) 364–371.

doi:10.1016/j.jmapro.2017.11.016.

[26] M.C. Araújo, C.M. Costa, S. Lanceros-Méndez, Evaluation of dielectric models for ceramic/polymer composites: Effect of filler size and concentration, J. Non. Cryst. Solids. 387 (2014) 6–15. doi:10.1016/j.jnoncrysol.2013.12.005.

[27] M. Lombardi, A. Guerriero, G. Kortaberria, I. Mondragon, M. Sangermano, L. Montanaro, Effect of the Ceramic Filler Features on the Properties of Photopolymerized BaTiO3-Acrylic Composites, Polym. Compos. 32 (2011) 1304–1312. doi:10.1002/pc.21154.

[28] H. Singh Nalwa, Handbook of Low and High Dielectric Constant. Materials and Their Applications, 1st Editio, Academic Press, London, England, 1999. http://www.ghbook.ir/index.php?name=های رسانه و فرهنگ نوین&option=com_dbook&task=readonline&book_id=13650&page=73&chkhashk=ED9C9491B4&Itemid=218&lang=fa&tmpl=component.

[29] P. Barber, S. Balasubramanian, Y. Anguchamy, S. Gong, A. Wibowo, H. Gao, H.J. Ploehn, H.C. Zur Loye, Polymer composite and nanocomposite dielectric materials for pulse power energy storage, 2009. doi:10.3390/ma2041697.

[30] H.C. Pant, M.K. Patra, A. Verma, S.R. Vadera, N. Kumar, Study of the dielectric properties of barium titanate-polymer composites, Acta Mater. 54 (2006) 3163–3169. doi:10.1016/j.actamat.2006.02.031.

[31] R.K. Goyal, V. V. Madav, P.R. Pakankar, S.P. Butee, Fabrication and properties of novel polyetheretherketone/ barium titanate composites with low dielectric loss, J. Electron. Mater. 40 (2011) 2240–2247. doi:10.1007/s11664-011-1743-5.

[32] Z. Yang, H. Peng, W. Wang, T. Liu, Crystallization behavior of poly(ε-caprolactone)/layered double hydroxide nanocomposites, J. Appl. Polym. Sci. 116 (2010) 2658–2667. doi:10.1002/app.

[33] S.F. Mendes, C.M. Costa, C. Caparros, V. Sencadas, S. Lanceros-Méndez, Effect of filler size and concentration on the structure and properties of poly(vinylidene fluoride)/BaTiO 3 nanocomposites, J. Mater. Sci. 47 (2012) 1378–1388. doi:10.1007/s10853-011-5916-7.

[34] H.I. Hsiang, K.Y. Lin, F.S. Yen, C.Y. Hwang, Effects of particle size of BaTiO3 powder on the dielectric properties of BaTiO3/polyvinylidene fluoride composites, J. Mater. Sci. 36 (2001) 3809–3815. doi:10.1023/A:1017946405447.

[35] S.W. Kim, H.R. Choi, C.S. Han, D. Bin Kim, J.W. Kim, Y.S. Cho, Dielectric and

current-voltage characteristics of flexible Ag/BaTiO3 nanocomposite films processed at near room temperature, RSC Adv. 7 (2017) 56038–56043. doi:10.1039/c7ra11640c.

[36] T. Nardi, M. Sangermano, Y. Leterrier, P. Allia, P. Tiberto, J.A.E. Månson, UV-cured transparent magnetic polymer nanocomposites, Polymer (Guildf). 54 (2013) 4472–4479. doi:10.1016/j.polymer.2013.06.052.

[37] E. Lizundia, A. Maceiras, J.L. Vilas, P. Martins, S. Lanceros-Mendez, Magnetic cellulose nanocrystal nanocomposites for the development of green functional materials, Carbohydr. Polym. 175 (2017) 425–432. doi:10.1016/j.carbpol.2017.08.024.

[38] M. Sangermano, G. Matucelli, E. Amerio, R. Bongiovanni, A. Priola, A. Di Gianni, B. Voit, G. Rizza, Preparation and characterization of nanostructured TiO2/epoxy polymeric films, Macromol. Mater. Eng. 291 (2006) 517–523. doi:10.1002/mame.200500420.

[39] P. Cardoso, J. Silva, D. Klosterman, J.A. Covas, F.W.J. van Hattum, R. Simoes, S. Lanceros-Mendez, The role of disorder on the AC and DC electrical conductivity of vapour grown carbon nanofibre/epoxy composites, Compos. Sci. Technol. 72 (2012) 243–247. doi:10.1016/j.compscitech.2011.11.008.

[40] J. Silva, S. Lanceros-Mendez, R. Simoes, Effect of cylindrical filler aggregation on the electrical conductivity of composites, Phys. Lett. Sect. A Gen. At. Solid State Phys. 378 (2014) 2985–2988. doi:10.1016/j.physleta.2014.08.011.

[41] E.S. Jang, S.B. Khan, J. Seo, Y.H. Nam, W.J. Choi, K. Akhtar, H. Han, Synthesis and characterization of novel UV-curable polyurethane-clay nanohybrid: Influence of organically modified layered silicates on the properties of polyurethane, Prog. Org. Coatings. 71 (2011) 36–42. doi:10.1016/j.porgcoat.2010.12.007.

[42] G. Trovati, E.A. Sanches, S.C. Neto, Y.P. Mascarenhas, G.O. Chierice, Characterization of Polyurethane Resins by FTIR, TGA, and XRD, J. Appl. Polym. Sci. 115 (2010) 263–268. doi:10.1002/app.31096.

[43] R.W. Arcís, A. López-Macipe, M. Toledano, E. Osorio, R. Rodríguez-Clemente, J. Murtra, M.A. Fanovich, C.D. Pascual, Mechanical properties of visible light-cured resins reinforced with hydroxyapatite for dental restoration, Dent. Mater. 18 (2002) 49–57. doi:10.1016/S0109-5641(01)00019-7.

[44] A.A. Zandinejad, M. Atai, A. Pahlevan, The effect of ceramic and porous fillers on the mechanical properties of experimental dental composites, Dent. Mater. 22 (2006) 382–387. doi:10.1016/j.dental.2005.04.027.

[45] M. Rincón-Iglesias, E. Lizundia, S. Lanceros-Méndez, Water-Soluble Cellulose Derivatives as Suitable Matrices for Multifunctional Materials, Biomacromolecules. (2019). doi:10.1021/acs.biomac.9b00574.

[46] X. Cao, H. Dong, C.M. Li, New nanocomposite materials reinforced with flax cellulose nanocrystals in waterborne polyurethane, Biomacromolecules. 8 (2007) 899–904. doi:10.1021/bm0610368.

[47] P. Costa, J. Silva, V. Sencadas, R. Simoes, J.C. Viana, S. Lanceros-Méndez, Mechanical, electrical and electro-mechanical properties of thermoplastic elastomer styrene-butadiene-styrene/multiwall carbon nanotubes composites, J. Mater. Sci. 48 (2013) 1172–1179. doi:10.1007/s10853-012-6855-7.

[48] J.F. Capsal, C. Pousserot, E. Dantras, J. Dandurand, C. Lacabanne, Dynamic mechanical behaviour of polyamide 11/Barium titanate ferroelectric composites, Polymer (Guildf). 51 (2010) 5207–5211. doi:10.1016/j.polymer.2010.09.011.

[49] T. Trzepiecinski, M. Gromada, Characterization of mechanical properties of barium titanate ceramics with different grain sizes, Mater. Sci. Pol. 36 (2018) 151–156. doi:10.1515/msp-2018-0009.

[50] D.M. Correia, R. Sabater i Serra, J.A. Gómez Tejedor, V. de Zea Bermudez, A. Andrio Balado, J.M. Meseguer-Dueñas, J.L. Gomez Ribelles, S. Lanceros-Méndez, C.M. Costa, Ionic and conformational mobility in poly(vinylidene fluoride)/ionic liquid blends: Dielectric and electrical conductivity behavior, Polymer (Guildf). 143 (2018) 164–172. doi:10.1016/j.polymer.2018.04.019.

[51] A.C. Lopes, C.M. Costa, R.S.I. Serra, I.C. Neves, J.L.G. Ribelles, S. Lanceros-Méndez, Dielectric relaxation, ac conductivity and electric modulus in poly(vinylidene fluoride)/NaY zeolite composites, Solid State Ionics. 235 (2013) 42–50. doi:10.1016/j.ssi.2013.01.013.

[52] L. Gu, T. Li, Y. Xu, C. Sun, Z. Yang, D. Zhu, D. Chen, Effects of the particle size of BaTiO 3 fillers on fabrication and dielectric properties of BaTiO 3 /Polymer/Al films for capacitor energy-storage application, Materials (Basel). 12 (2019). doi:10.3390/ma12030439.

[53] R.K. Goyal, S.S. Katkade, D.M. Mule, Dielectric, mechanical and thermal properties of polymer/BaTiO 3 composites for embedded capacitor, Compos. Part B Eng. 44 (2013) 128–132. doi:10.1016/j.compositesb.2012.06.019.

[54] K. Suematsu, M. Arimura, N. Uchiyama, S. Saita, T. Makino, Synthesis of

BaTiO3/polymer composite ink to improve the dielectric properties of thin films, Compos. Part B Eng. 104 (2016) 80–86. doi:10.1016/j.compositesb.2016.08.011.

[55] Y. Bai, Z.Y. Cheng, V. Bharti, H.S. Xu, Q.M. Zhang, High-dielectric-constant ceramic-powder polymer composites, Appl. Phys. Lett. 76 (2000) 3804–3806. doi:10.1063/1.126787.

[56] R.K. Goyal, A.B. Kulkarni, Electrical properties of novel three-phase polymer nanocomposites with a high dielectric constant, J. Phys. D. Appl. Phys. 45 (2012). doi:10.1088/0022-3727/45/46/465302.

[57] D.J. Bergman, The dielectric constant of a composite material-A problem in classical physics, Phys. Rep. 43 (1978) 377–407. doi:10.1016/0370-1573(78)90009-1.

[58] C.W. Nan, Comment on "Effective dielectric function of a random medium," Phys. Rev. B - Condens. Matter Mater. Phys. 63 (2001) 5–7. doi:10.1103/PhysRevB.63.176201.

[59] T. Furukawa, K. Ishida, E. Fukada, Piezoelectric properties in the composite systems of polymers and PZT ceramics, J. Appl. Phys. 50 (1979) 4904–4912. doi:10.1063/1.325592.

[60] N. Jayasundere, B. V. Smith, Dielectric constant for binary piezoelectric 0-3 composites, J. Appl. Phys. 73 (1993) 2462–2466. doi:10.1063/1.354057.

[61] C. Kittel, Introduction to Solid State Physics, Eighth Edi, Phoenix, EEUU, 2005. doi:10.1021/ja01569a094.

[62] G.F. Dionne, J.F. Fitzgerald, R.C. Aucoin, Dielectric constants of paraffin-wax-TiO2 mixtures, J. Appl. Phys. 47 (1976) 1708–1709. doi:10.1063/1.322753.

[63] W.R. Tinga, W.A.G. Voss, D.F. Blossey, Generalized approach to multiphase dielectric mixture theory, J. Appl. Phys. 44 (1973) 3897–3902. doi:10.1063/1.1662868.

[64] T. Yamada, T. Ueda, T. Kitayama, Piezoelectricity of a high-content lead zirconate titanate/polymer composite, J. Appl. Phys. 53 (1982) 4328–4332. doi:10.1063/1.331211.

[65] Z. Ahmad, A. Prasad, K. Prasad, A comparative approach to predicting effective dielectric, piezoelectric and elastic properties of PZT/PVDF composites, Phys. B Condens. Matter. 404 (2009) 3637–3644. doi:10.1016/j.physb.2009.06.009.

[66] S. Aldrich, Sigma Aldrich - Barium titanate (IV), materials datasheet 2019, (n.d.). https://www.sigmaaldrich.com/catalog/product/aldrich/467634?lang=es&region=ES (accessed November 20, 2019).